Geophys. J. Int. (2009) **176,** 657–669 doi: 10.1111/j.1365-246X.2008.03990.x

The 2007 Pisco, Peru, earthquake (*M*8.0): seismology and geodesy

Juliet Biggs,[1] David P. Robinson[2] and Timothy H. Dixon[1]

[1] *Rosenstiel School of Marine and Atmospheric Sciences, University of Miami, FL, USA. E-mail: jbiggs@rsmas.miami.edu*
[2] *Department of Earth Sciences, University of Oxford, UK*

Accepted 2008 September 24. Received 2008 September 24; in original form 2008 June 13

SUMMARY

We investigate the 2007 Pisco, Peru, earthquake (*M*8.0) using seismological and geodetic data. Analysis of teleseismic records indicates that the earthquake is characterized by a steadily increasing moment rate, with the maximum occurring between about 55 and 70 s and the associated slip occurring about 40 km south of the epicentre. We combine InSAR data from L-band (ALOS) and C-band (Envisat) satellites to produce a 3-D image of the ground displacements caused by the earthquake. Distributed slip inversions of the interferograms identify a single large patch of slip in the location of the maximum moment rate identified by seismology. Despite a clear spatial coincidence between the location of the coseismic slip and the anomalously high topography of the Paracas Peninsula, we find no evidence that the earthquake was directly responsible for motion on any upper plate faults.

Key words: Satellite geodesy; Earthquake dynamics; Subduction zone processes; South America.

1 INTRODUCTION

Subduction zone processes occur on a range of timescales from the generation of seismic waves to the building of mountain chains. Great earthquakes involve slip on the plate interface of up to 15 m or more (e.g. 2004 Sumatra–Andaman earthquake; Lay *et al.* 2005). In most cases, earthquake processes are better understood by considering both seismic and geodetic information together (e.g. Biggs *et al.* 2006; Chlieh *et al.* 2008; Pritchard & Fielding 2008). Historical seismicity can give information about the location and geometry of existing faults. Teleseismic body waves give detailed information about the temporal evolution of slip, but due to the large source–receiver distances, can have low spatial resolving power. Conversely, image-based geodetic techniques such as InSAR provide a spatially dense measurement of terrestrial surface displacement, which offer excellent constraint on fault location, geometry and slip distribution for continental earthquakes but may have a repeat time on the order of months. The resulting slip distributions are not always consistent (Wald *et al.* 1996), either because processes with different timescales are responsible (Pritchard *et al.* 2007) or because of differences in inversion techniques or different data noise characteristics (Segall & Davis 1997). Joint inversions using both data sets do not necessarily address these problems (Funning *et al.* 2005; Pritchard *et al.* 2007).

On much longer timescales, subduction zones may also generate significant permanent deformation and topography. Geodetic measurements indicate long-term shortening of 5–15 mm yr^{-1} across the Andes (Norabuena *et al.* 1998; Bevis *et al.* 2001), whereas geomorphological and palaeobotanical evidence implies surface uplift of 2300–3400 m since late Miocene time, requiring long-term average uplift rates of 0.2–0.3 mm yr^{-1} (Gregory-Wodzicki 2000). The mechanisms by which subduction zones generate topography are poorly understood. In current models, elastic strain accumulated on the upper plate during the interseismic phase is completely released during an earthquake, resulting in zero net deformation (Savage 1983). Recent studies have shown a correlation between interseismic coupling and large seismic asperities, which suggests these may be consistent features (Chlieh *et al.* 2008). Furthermore, these patches also correlate with geomorphic features (such as outer arc islands in Sumatra), suggesting they influence long-term topographic development.

We investigate the 2007 *M*8.0 Pisco, Peru, earthquake, presenting new InSAR-based geodetic data and teleseismic data on this major plate boundary event.

2 TECTONIC SETTING

2.1 Historical earthquakes

Historical reports along the coast of Peru (Dorbath *et al.* 1990) reveal three distinct zones of earthquake behaviour (Fig. 1a). The central region (10°S–14°S) is bounded by topographic features on the subducting plate, the Mendaña fracture zone to the north and the Nazca ridge to the south. The distribution of large historical earthquakes shows irregular behaviour both in space and time, making estimates of earthquake repeat times impractical. Three possible rupture modes—dividing the zone into 1, 2 or 3 segments—are all represented historically. In the central region, the largest possible earthquake (*M*8.5), rupturing the entire zone, last occurred in 1746 and was followed by two centuries of quiescence before activity recommenced in 1940.

Seismological studies of recent large earthquakes along the Peru coast (*M*8.0; 1996 *M*7.7; 1942 *M*8.1; 2001 *M*8.4; 2001 *M*7.6)

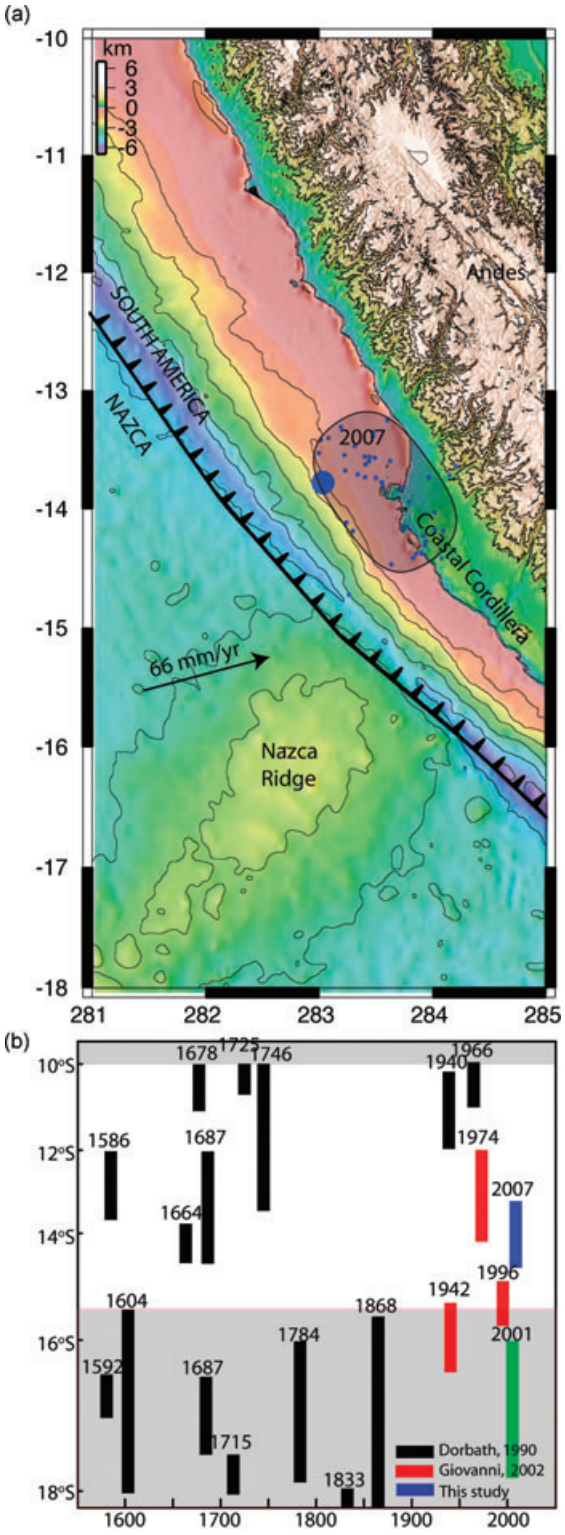

Figure 1. (a) Topography/Bathymetry of central Peru, showing the Nazca Ridge, the Andes, the trench and the location of the 2007 Pisco, Peru, earthquake. The shaded region represents the aftershock zone, based on the National Earthquake Information Centre (NEIC) catalogue. The plate convergence vector is taken from the global model for recent plate velocities (REVEL; Sella *et al.* 2002). (b) Historical earthquakes in central and south Peru. Updated from Dorbath *et al.* (1990). Shading represents the three identified segments (northern-grey; central-white; southern-grey).

show the following common features: (1) unilateral rupture to the southeast; (2) the largest pulse of moment release occurs late in the rupture history, often 60 s or more after the earthquake initiation; and (3) the region of high moment release is small in relation to the fault area as defined by aftershocks (Swenson & Beck 1996; Giovanni *et al.* 2002; Pritchard *et al.* 2007).

2.2 The 2007 earthquake

The most recent earthquake in this sequence occurred August 15, with an estimated magnitude of 8.0 (Fig. 1b). The earthquake caused widespread damage; peak intensities reached VII–VIII (MMI) in the towns of Chincha Alta and Ica, with 595 people killed and 318 missing (Tavera & Bernal 2008). A tsunami was observed both locally (∼1 m at Callao and La Punta, Peru, across the Pacific (≤25 cm in New Zealand) and on a deep pressure sensor off the coast of Chile (Fritz *et al.* 2007). Field investigations report uplift and subsidence along the coastline that did not exceed the tidal range ∼40 cm and found no evidence for re-activation of the faults on the Paracas Peninsula (Audin *et al.* 2007). Pritchard & Fielding (2008) perform a joint inversion of InSAR and teleseismic data and conclude that the slip maximum occurred 60–90 s after the main shock started and about 70 km from the hypocenter, suggesting an extremely low rupture velocity ($<1.5\,\mathrm{km\,s^{-1}}$) or long slip rise time.

3 INTERFACE GEOMETRY

InSAR measures surface displacements on land, so for subduction zones, where the subducting plate is underwater, observations are only possible on one side of the fault. Consequently, many uncertainties remain in the fault geometry, with large trade-offs between earthquake slip, dip and rake. External information is traditionally used to determine the interface geometry.

Based on microearthquake studies, the average dip of the interface between the South American and Nazca plates is estimated to be 20°–25° (Grange *et al.* 1984) from the trench to depths of about 100 km, beyond which is a flat seismic zone about 25 km thick (Suárez *et al.* 1990). However, a more detailed description of the shape of the upper, locked portion is important for modelling the earthquake slip distribution. Spence *et al.* (1999) suggest a hinge in the plate at 25 km depth, where the slab dip changes from 10°–12° to 25°–55°. Norabuena *et al.* (1998) use a standardized geometry for the whole of the Central Andes, with a dip of 10° to 15 km depth, 18° at depths of 15–35 km and 26° from 35–50 km. The study area is characterized by subduction of the Nazca Ridge, a region of thickened, relatively buoyant oceanic crust. Thus, we expect the dip of the shallow part of the subduction zone here to be shallower than regions to the north and south.

3.1 Earthquake relocations

In order to fit the local, rather than regional, subduction interface, we use a joint hypocentral determination (JHD) to relocate the 384 earthquakes recorded in the ISC catalogue between 1990 and 2005 for a 2° square region, centred on the Pisco epicentre. The *M*7.7 earthquake on the 1996 November 12 is used as the reference event. Of the 384 earthquakes recorded, 277 were relocated. Of these 64 had 90 per cent error ellipsoids in the range ≤50 km and 123 had ellipsoids in the range 50–100 km. The horizontal location is

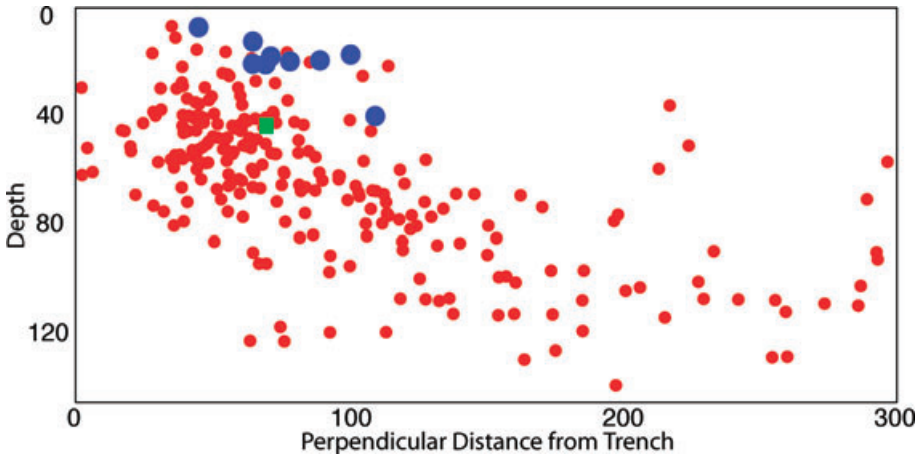

Figure 2. Cross-section through slab seismicity for the Pisco area. A Joint hypocentral determination (JHD) is used to relocate the 384 earthquakes recorded in the ISC catalogue between 1990 and 2005 for a 2° square region centred on the Pisco epicentre. Blue dots show the location of aftershocks from Tavera & Bernal (2008). The reference event (1996 November 12 M7.7) is shown as a green square.

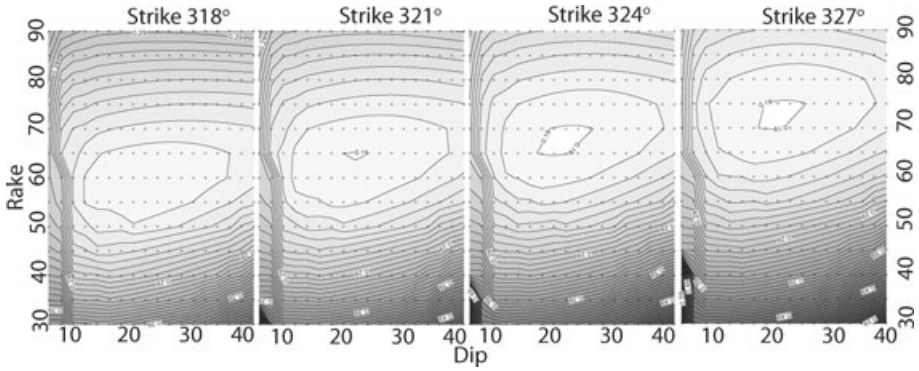

Figure 3. CMT solution space of the 2007 Pisco earthquake, showing the broad range of values of strike, dip and rake for which there are solutions with misfit values only marginally higher than the global minimum.

significantly better constrained than the vertical location, so that 190 events have 90 per cent error ellipses (the projection of the error ellipsoids onto the earth's surface) $\leq$50 km and 36 have ellipses $\leq$20 km. The earthquakes are plotted according to perpendicular distance from the trench (Fig. 2) and show the broad shape of the subducting plate. However, the interface geometry remains poorly defined due largely to the poorly constrained depth of events. A wide range of dip values would produce an acceptable fit to the data. It is possible the diffuse nature of the seismicity reflects lateral variation in the slab geometry, but the location errors are too large to justify splitting the region into smaller areas with fewer earthquakes. Furthermore, there is likely to be a degree of seismicity in the overlying plate, so that the earthquakes do not form a single 2-D interface in the classical plate boundary sense. In the course of time, a larger number of better-located earthquakes will occur, hence improving this picture. In Sections 3 and 4, we test possible geometries with geodetic and seismological inversions for the 2007 earthquake.

4 SEISMOLOGY

4.1 Long-period seismology

The global Centroid Moment Tensor (CMT) solution (strike 321°, dip 28°, rake 63°, M_0 1.12×10^{21} N m) has a fault plane with a dip significantly higher than is suggested for the upper portion of the subduction interface in this region (see Section 3). For this reason, and to investigate the robustness of the long-period solution, we recalculate the CMT solution. By analysis of mantle wave data from 179 channels and 80 stations, we find a CMT solution of strike 324°, dip 22°, rake 68°, M_0 1.07×10^{21} N m in close agreement with the global CMT solution. Next, we investigate the solution space in the vicinity of the optimal solution by applying the pure double couple constraint and inverting to find centroid location (in four dimensions) and moment over a range of fixed strike, dip and rake (Henry *et al.* 2002). Unlike shallow strike-slip earthquakes, dip-slip earthquakes are not expected to have unstable CMT solutions (Henry *et al.* 2002; Robinson *et al.* 2006a), and this is shown to be true in this case with the results of the grid search shown in Fig. 3.

The results show that there is an extremely broad range of values of strike, dip and rake for which there are solutions with misfit values only marginally higher than the global minimum. Strikes between about 318° and 327° are clearly possible, as are dips anywhere between ~10° and ~40°. A similarly broad range of rakes is permitted by the data. Interestingly, there is a strong trade-off between the moment and dip of the solutions found, with an almost exponential growth in moment as dip is decreased, shown in Fig. 10(a). Thus, if we conclude that the causative fault plane of this earthquake is shallower than that indicated by the global CMT solution, then the long-period seismological evidence is that the moment of the earthquake could have been larger than the reported value.

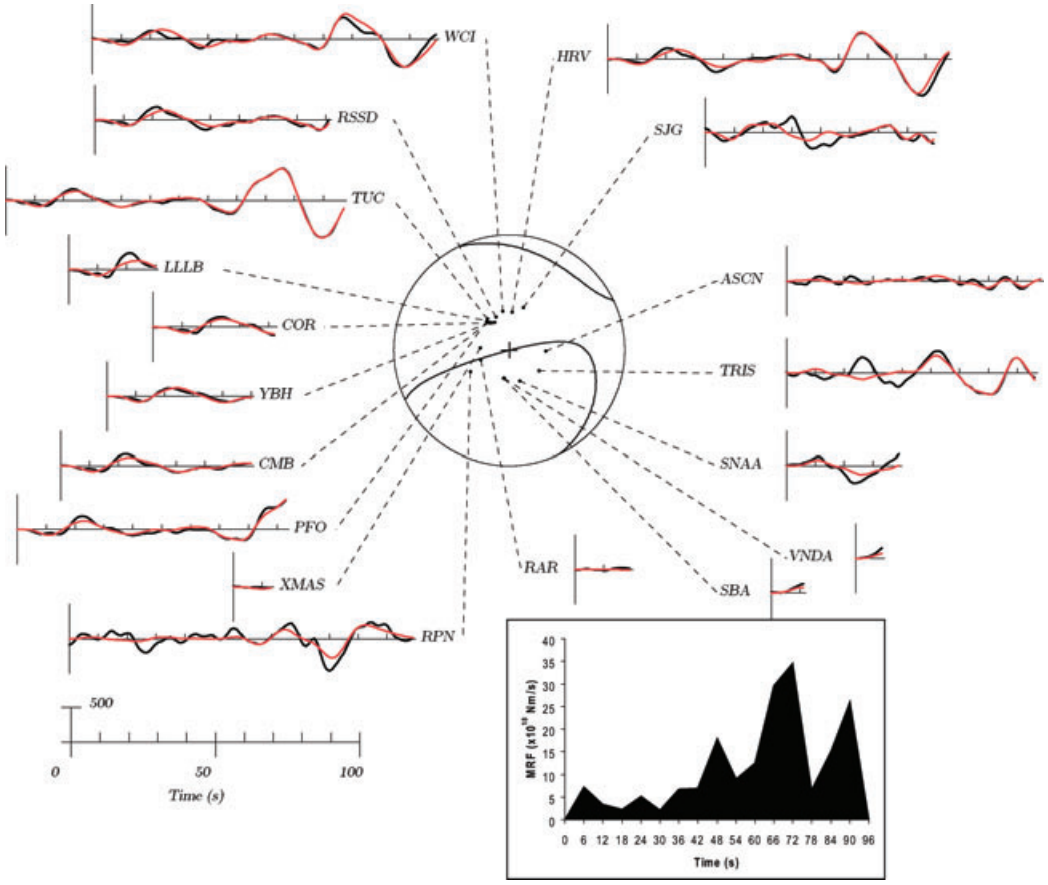

Figure 4. Real (black) and synthetic (red) seismograms for the 2007 Pisco, Peru, earthquake. We use broad-band *SH* records from 17 stations at epicentral distances between 50° and 90° . The synthetic seismograms are for the preferred solution shown in Fig. 5.

4.2 Short-period seismology

We analyse 18 *SH* broad-band seismograms at epicentral distances between 30° and 85°, using the method of Das & Kostrov (1990, 1994) to find the rupture history (Fig. 4). *SH* wave data are chosen as they do not suffer from water reverberations as *P* waves do. *S*-wave arrival times were picked by hand and recordings were terminated either at 120 s or just before the expected arrival times of unmodelled reflection phases such as *ScS* or *SS*. All the selected traces have usable durations of at least 10 s, with the majority longer than 80 s in length. As a result of the lower quantity of data used to analyse the later portions of the rupture history, the rupture process towards the end of the earthquake should be regarded as less reliable than the earlier portions. To model Green's functions, we use the crustal model CRUST 2.0 at the source and one modified from either CRUST 2.0 or CRUST 5.1 (Mooney *et al.* 1998), based on known local geological conditions, at the receiver. In the method of Das & Kostrov (1990), a specified fault plane is divided into a number of cells along strike and dip, and the rupture duration is split into a number of time steps. The rake is constant for all slip patches. Each cell is then permitted to slip in each time step, except when prohibited by causality constraints imposed. The synthetic seismograms produced are summed and compared with the real data.

The long-period solution discussed in the previous section provides a starting point for the broad-band solution. Initially, many inversions are performed with a variety of mechanisms close to that of the long-period solution. These initial inversions show that dips in excess of ∼15° are strongly unfavoured, with a mechanism of strike 324°, dip 12°, rake 70° being optimal. It was found that significant changes in strike are not permitted by the data and that the optimal value of rake is dependant on dip. These initial inversions also allow the testing of various causality constraints, and these tests show that, apart from numerical noise, there is no slip ahead of a *S* wave from the hypocentre. Despite recent observations of intersonic rupture propagation (Bouchon & Vallée 2003; Dunham & Archuleta 2004; Robinson *et al.* 2006a), such rupture velocities are not expected in mode III faulting such as is present here (Rosakis *et al.* 1999). Hence for the final inversions we impose this condition as the causality constraint.

The mechanism of the best-fitting broad-band solution—strike 324°, dip 12°, rake 70°—is still in the broad region of low misfit of the long-period solutions (Fig. 3); thus, it seems likely that this mechanism is more representative of the rupture than the published global CMT solution. This also agrees well with the InSAR solutions, which, although subject to similar trade-offs, are strongly suggestive of a very shallowly dipping fault plane (see Section 5). This preference for solutions with relatively shallow dip is in agreement with our expectation that the plate interface near the bouyant Nazca Ridge subducts at shallow angle compared with regions north and south and consistent with the modelled subduction zone geometry of Tavera & Bernal (2008).

Previous authors have suggested a more complex geometry for the subduction interface (Section 3). We investigate whether the data could be better modelled by considering two or more faults connected at depth, with each sucessively deeper fault dipping at a

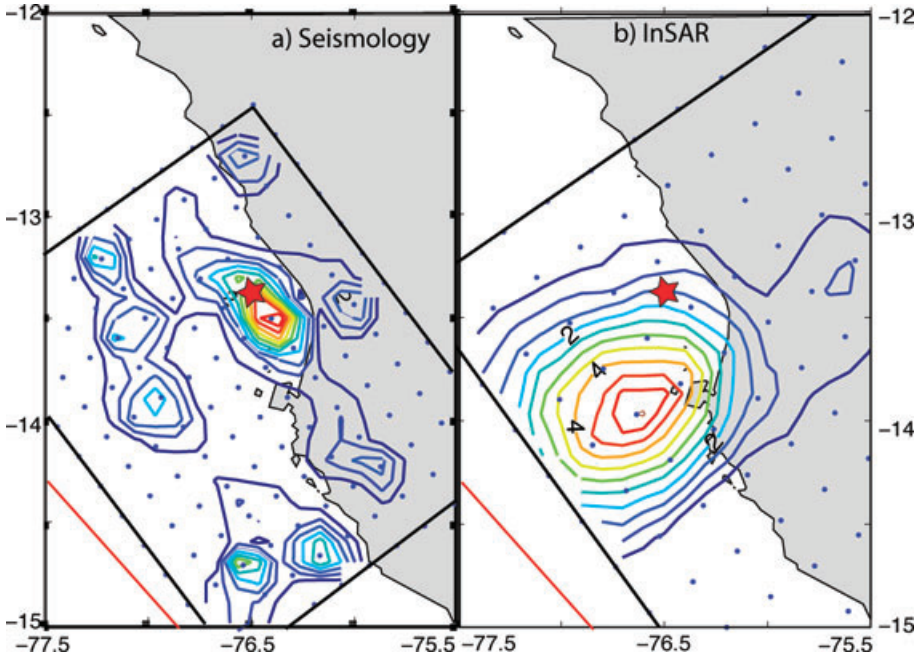

Figure 5. Slip distribution for the 2007 Pisco, Peru, earthquake from (a) seismology and (b) geodesy. The fault plane dips at 12° northwest. Contours are shown every 50 cm, up to the peak slip of ∼5 m. The peak slip lies south of the epicentre, offshore of the Paracas Penninsula, in both slip distributions but the seismological solution places the peak slip close to the epicentre (north of the Paracas Penninsula) whereas the InSAR solution places the peak slip due west of the Paracas Penninsula. The geodetic solution is much smoother than the seismology solution. Trench location is shown in red. The surface projection of the fault plane lies land ward of the trench location due to a shallowing dip to 5°–8° (Krabbenhöft *et al.* 2004) close to the surface.

higher angle to approximate the bending of the subduction interface. Initially, a two-fault model was considered, with the upper 20 km dipping at 12°, with a dip of 33° below that (Spence *et al.* 1999). This model failed to produce solutions with improved misfit over the single fault model. Then a three-fault model was investigated: with the fault dipping at 12° at depths less than 15 km; at 18° between 15 and 35 km and at 26° at depths greater than 35 km (Norabuena *et al.* 1998). Again this failed to produce solutions with significantly better misfit than the single fault model. This leads to the conclusion that a single, shallowly dipping fault plane is a satisfactory model to adopt.

Next, we attempt to determine the optimum moment for the broad-band solution. The long-period data suggest that the total moment should be somewhere in the region of 1.11–1.61 $\times$ 10^{21} N m, the upper and lower bounds being the value for moment found for an earthquake with the prescribed mechanism and the optimal moment, respectively. Solutions with both of these moments were sought. The solutions with lower moment place the region of maximum slip close to the hypocentre, just off the coast of Peru close to the Paracas Peninsula. The solutions with higher moment place the additional moment as large slip directly under the coast of Peru, to the immediate north of the earthquake hypocentre and as extra slip close to the subduction trench. The solutions with higher moment are at odds with the InSAR solutions, which are strongly suggestive of there being little or no slip under the Peruvian coast, and at odds with the fact that only a subdued tsunami was formed. Thus, our preferred seismological solution has moment of 1.11 $\times$ 10^{21} N m and is shown in Figs 5(a) and 6.

From the large number of solutions obtained in determining the fault geometry, we find that the moment rate function (MRF) is highly stable and robust. This is a common feature across almost all seismological studies. For this earthquake, the MRF shows a general increase in moment rate up to ∼75 s with the majority of moment occuring between ∼55 and 70 s (Fig. 4). The residents of Lima reported two distinct episodes of shaking, separated by about 1 min, leading many to infer two separate patches of slip. However, this effect could also be caused by the same patch slipping multiple times or interactions caused by the exact geometry and slip history. Our synthetic seismograms reproduce this observation in the *SH* waves whereas still maintaining a simple moment release function (MRF), with stations in the north (HRV, WCI and TUC) showing two 'pulses' of intensity separated by about a minute.

The early parts of the rupture history have slip concentrated in the hypocentral region and updip of the hypocentre. The main moment occurence between ∼55 and 70 s is concentrated relatively close to the hypocentre, about 40 km to its south, just to the west of the Paracas Peninsula (Fig. 6). Peak slip is in the region of 6 m. Robustness tests show that due to the low number of stations used in this inversion, the location of the main moment release is not well constrained, although its location in the preferred solution shown in Fig. 5 is close to the peak slip seen in the InSAR solution.

Our results shows notable differences from the published slip distributions of Pritchard & Fielding (2008) due to differences in data selection and model assumptions. The method of Ji *et al.* (2002) used by Pritchard & Fielding (2008) imposes a 'rupture front and healing front' constraint, which implies slip can only continue for a set period of time after the rupture front has passed. We find that significant slip occurred close to the hypocentre, relatively late in the rupture history (60–90 s) of the Pisco earthquake. It is likely that the healing front constraint prevented this scenario from occurring in the model of Pritchard & Fielding (2008).

Second, we terminate seismograms when core reflection phases arrive. Although frequently considered to be of smaller magnitude than direct phases, they may be comparable if the direct phase is close to a nodal plane but the reflected phase is not. In the model

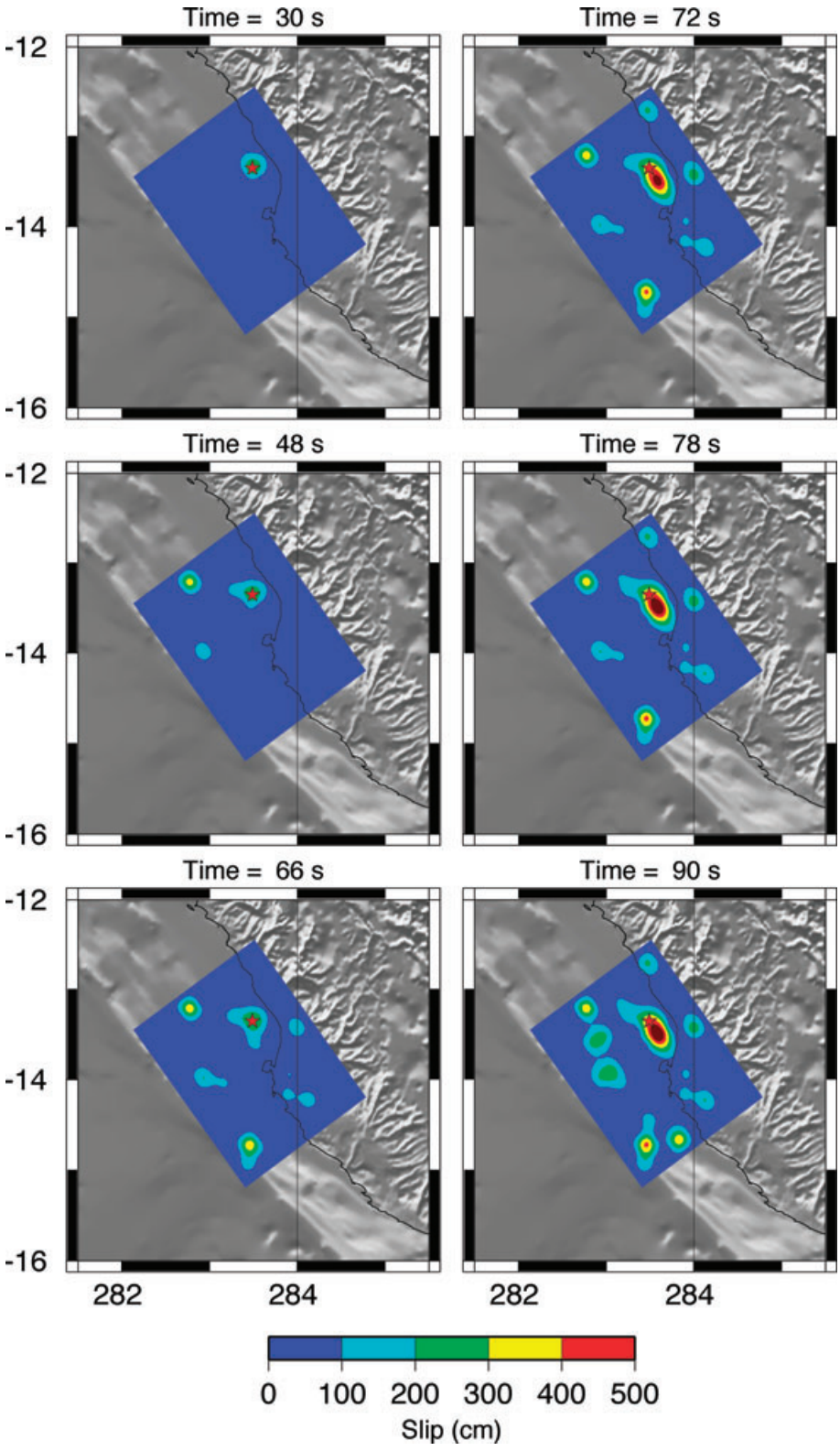

Figure 6. Cumulative slip distribution at selected intervals during the earthquake, showing the a general increase in moment rate up to about 75 s with the majority of moment occurring between ~55 and 70 s. The early parts of the rupture history have slip concentrated in the hypocentral region and updip of the hypocentre. The main moment occurrence between ~55 and 70 s is concentrated relatively close to the hypocentre, just to the west of the Paracas Penninsula.

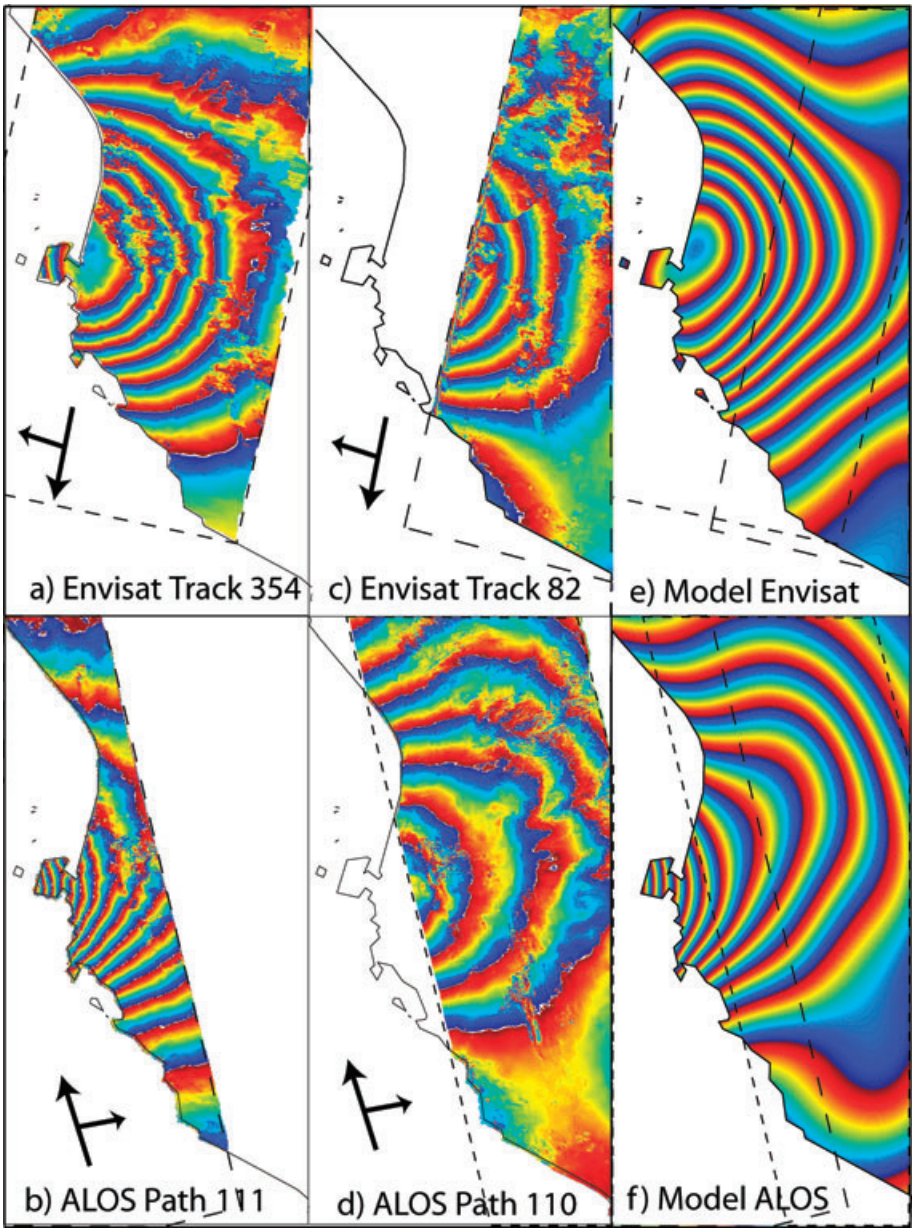

Figure 7. Interferograms and models showing the line-of-sight surface displacements from the 2007 Pisco, Peru, earthquake. (a) Interferogram Envisat track 354, (b) inteferogram ALOS track 111, (c) interferogram Envisat track 82, (d) interferogram ALOS track 111, (e) model surface displacements projected into Envisat line of sight and (f) model surface displacements projected into ALOS line of sight.

of Pritchard & Fielding (2008), the inclusion of the core reflection phases causes a some degradation of the fit to the *S*-wave data compared with the *P*-wave data (since *ScS* is larger in comparison to *S* than *PcP* is to *P*), especially after the theoretical *ScS* arrival time, but it is not possible to determine the exact effect on the resulting slip distribution.

5 GEODESY (InSAR)

5.1 Data

We measure surface displacement using SAR interferograms constructed using radar images from the Envisat and ALOS satellites. Each interferogram produces a spatially dense grid of 1-D measurements of displacement in the direction of the satellite line of sight (Fig. 7). The interferograms used in this study are taken from different pass directions (Table 1), so together, give information about the full 3-D displacement field (Wright *et al.* 2004). The interferograms were processed using the ROI_PAC software packages (Rosen *et al.* 2004) and topography removed using a Digital Elevation Model (DEM) from the Shuttle Radar Topography Mission (SRTM; Farr 2007). The coastal plain of Peru is an arid, desert region and the interferometric coherence is excellent in both C-band (Figs 7a and c) and L-band (Figs 7b and d). Despite time spans of up to 4 yr, decorrelation occurs only over small areas of shifting sand dunes.

All interferograms show a circular pattern of displacements centred close to the Paracas peninsula consistent with a single patch of earthquake slip (Fig. 7). The vertical component of the line of

Table 1. Interferograms used in this study. The letter in brackets represents the satellite radar band: C-band has a wavelength of 5.6 cm and L-band has a wavelength of 23.6 cm. Line of sight is defined by the unit vector [East, North, Up] and dates are given in YY/MM/DD format.

Satellite	Track	Line of sight	Date1	Date 2	$B_\perp$
ALOS (L)	111	[−0.61, −0.13, 0.78]	07/07/12	07/08/27	126
ALOS (L)	110	[−0.61, −0.13, 0.78]	07/08/10	07/09/25	428
Envisat (C)	125	[+0.43, −0.08, 0.90]	03/10/10	07/10/19	−37
Envisat (C)	82	[+0.43, −0.08, 0.90]	03/07/13	07/08/26	198

sight is roughly equal for both ascending and descending tracks but the east–west component is reversed (Table 1). Consequently, the descending interferograms (Figs 7a and c) show range increase (e.g. the Paracas peninsula moves away from the satellite), whereas the ascending interferograms (Figs 7b and d) show range decrease. The 'bulls-eye' displacement pattern of fringes is characteristic of earthquakes in which only small amounts of slip occurred close to the surface. The centre of the 'bull's eye' appears to shift between descending and ascending passes because the horizontal and vertical components combine differently according to the line-of-sight vector (Table 1).

Interferograms show the total surface displacement between the two radar images. The pre-earthquake images for the Envisat interferograms date from 2003 and include ∼4 yr of interseismic deformation in addition to the coseismic deformation. We use a backslip model of interseismic slip at subduction zones (Savage 1983) to correct for displacements taking place before the earthquake. We base our model parameters on a GPS survey of the Central Andes (Norabuena *et al.* 1998), which found that on average only part (45 mm yr^{-1}) of the interplate motion (75 mm yr^{-1}) is locked on the subduction interface. This gives a maximum correction to the satellite line-of-sight displacement of 11 cm. Corrections using an updated South American reference frame (Bevis *et al.* 2001) yielded similar corrections. All post-earthquake images are from at least 12 days after the earthquake, during which time the most rapid

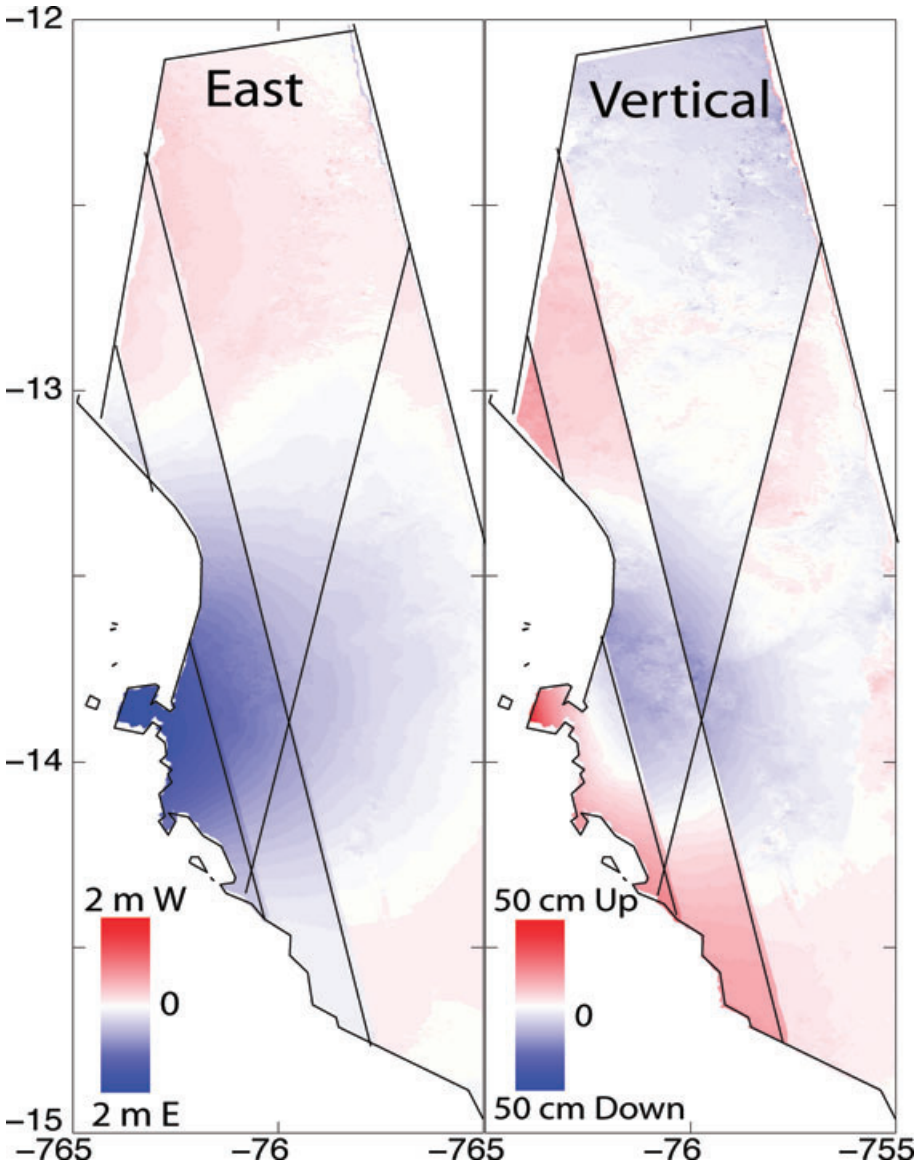

Figure 8. East and vertical components of surface displacements for the 2007 Pisco, Peru, earthquake. Displacement components are derived from ascending and descending interferograms. No direct assumptions about fault geometry (specifically dip) are required, but we assume the contribution to the line-of-sight vector from the north–south component of motion is negligible.

afterslip is expected to take place. Thus, we expect the moment estimated from InSAR to be larger than from seismology.

Since we have interferograms from two look directions (ascending and descending satellite passes), it is possible to separate two components of displacement. Since the earthquake slip vector is close to due west, and the line-of-sight displacements are only mildly affected by a north–south component (Table 1), we solve for the east and vertical components of displacement only. We use all four interferograms where possible, but at the minimum, require at least one descending and one ascending observation. The resulting displacement field (Fig. 8a) shows west directed horizontal motions up to a maximum of 3.6 m and a complex pattern of uplift and subsidence, with ∼50 cm of uplift on the Paracas Peninsula and a broad area of subsidence on land. Discontinuities along the track edges are caused by long wavelength errors due to orbital uncertainties and the approximation of a fixed line of sight. The intermediate wavelength noise is likely to be caused by atmospheric effects. Although this 2-D field is superseded by a more complete modelled version in the next section, it does not rely on assumptions about the fault geometry, so, provides a more objective measurement of the vertical component.

5.2 Modelling

We use the *slipinv* code (Funning *et al.* 2005) to relate the line-of-sight surface displacements to slip on the fault plane at depth. The code performs a linear inversion for the amount of slip on a grid of fault elements, each with specified fault geometry. Green's functions are generated using the Okada solutions for surface displacement, caused by slip on a rectangular dislocation in an elastic half-space and assume a constant line-of-sight vector for each interferogram. The inversion is smoothed using a weighted Laplacian operator. The inversion simultaneously solves for fault slip and nuisance parameters on each interferogram. These include a long-wavelength orbital uncertainty, which is modelled using a 2-D quadratic polynomial and offsets between interferograms caused by the arbitrary choice of reference pixel. Before modelling, each interferogram is downsampled to ∼1000 points using the quadtree algorithm (Jonsson *et al.* 2002), which concentrates sample density in areas of high displacement gradient (Fig. 11).

Initially, we test a range of interface geometries and smoothing constraints (Fig. 10). The strike (324°) and rake (70°) of the subduction zone is taken from the orientation of the trench at the surface and the best-fitting broad-band seismological solution. We constrain the location of the fault using the trench location and depth (4 km).

Initially, we test a range of fault dips for a single fault geometry and find a broad minimum misfit for dips in the range 10°–14° (Fig. 10b), consistent with the seismological solutions. This also corresponds to a minimum in the moment of the solution and the dip at which the geodetic and seismological moments agree most closely (Fig. 10b). As with the seismology, we then test a more complex fault geometry, to see if this can reduce the misfit to the data. To simulate the curvature of the subducting plate, we use a combination of two fault planes, with the lower plane having a steeper dip than the upper plane (Fig. 9a). We carry out a grid search over three parameters: hinge depth, H; shallow plane dip, θ_1 and lower plane dip, θ_2. For each inversion, we estimate the combined root mean square misfit (Fig. 9b). The lowest misfits are found when both planes have a very shallow dip (8°–10°), and very high misfits are found when the dip increases with depth.

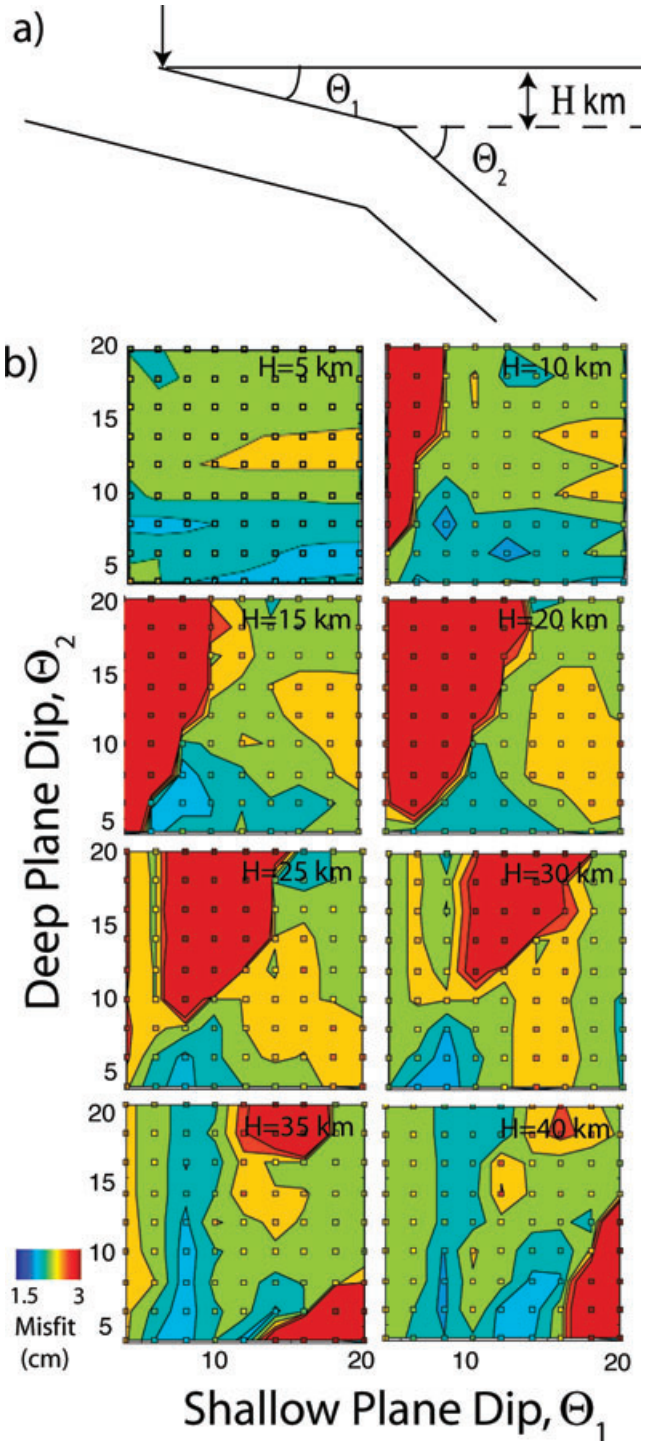

Figure 9. (a) Definition of parameters for 'curved' subduction geometry. The accuracy of earthquake relocations in this area is insufficient to define the interface geometry, so we carry out a grid search to find the best fitting hinge depth, H, shallow plane dip, θ_1, and deep plane dip, θ_2. (b) Results of grid search to find best fitting fault geometry for the Pisco earthquake. Hinge depth, H is varied between 5 and 40 km (plots a–h), with shallow plane dip, θ_1 (x-axis) and θ_2 (y-axis) between 4° and 20°. To satisfy increasing dip with depth, $\theta_2 \geq \theta_1$. Each square represents the misfit from a single experiment, which are then interpolated to provide the background colours and contours.

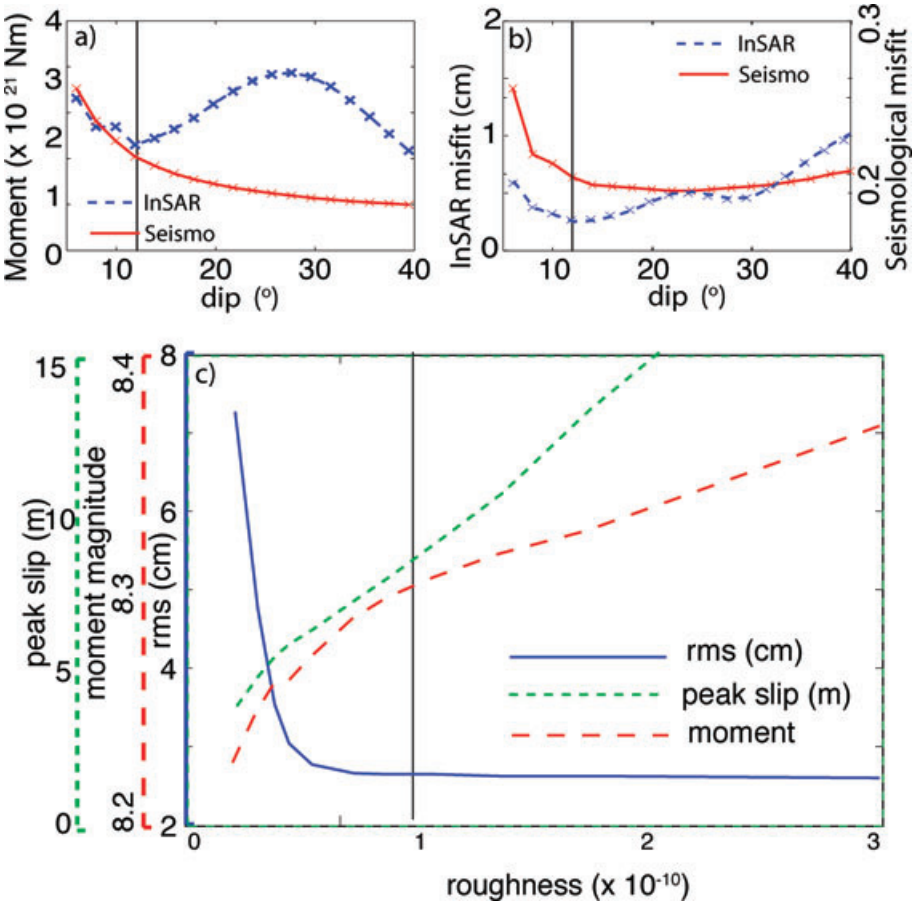

Figure 10. Sensitivity of the inversions to fault dip and smoothing parameter. (a) Trade-offs between fault dip and moment for the geodetic and long-period seismological solutions. (b) Trade-offs between fault dip and misfit for the geodetic and long-period seismological solutions. InSAR misfit is the root mean square misfit to the subsampled data. For the long-period seismology, the misfit is the variance ratio, defined as the ratio of the mean square misfit to the mean square data amplitude. (c) Effect of solution roughness on peak slip (green), moment (red) and root mean square misfit (blue). The chosen smoothing parameter is marked by the black line.

Distributed slip inversions are very sensitive to the choice of smoothing parameter. To illustrate the trade-offs involved, Fig. 10 plots solution roughness against root mean square misfit (blue), moment (red) and peak slip (green). The chosen smoothing parameter is shown by the vertical black line. In general smooth solutions have high misfits, low moment and low peak slip. The solution misfit shows little variation between rough solutions, but the peak slip can vary by a factor of 4 (between 4 and 15 m). We fix our choice of smoothing parameter so that the peak slip matches that determined using seismology (∼5–6 m) in contrast to the InSAR derived slip distribution of Pritchard & Fielding (2008), which has a higher peak slip of ∼8 m and their joint solution which has peak slip in excess of 15 m. For any reasonable smoothing parameter, the moment reaches a stable value of 2.5×10^{21} N m (M_0 8.27), higher than that found with seismology, 1.1×10^{21} N m (M_0 8.03).

The root-mean-square model misfits for the chosen solution (∼2.76 cm) are consistent with the magnitude expected from atmospheric noise and model geometry simplification. The residuals at the subsampled points for each iterferogram are shown in Fig. 11.

The inversion shows a circular pattern of slip, centred just offshore the Paracas peninsula, with a peak slip of ∼6.2 m at a depth of ∼10 km (Fig. 5). The peak slip is consistent with the amount of slip observed in other earthquakes of this magnitude and with results from the seismological inversions. The slip model is then used to predict the full 3-D surface displacement field, both onshore and offshore. All the tested models show the hinge line between uplift and subsidence lies along the coastline (Fig. 12). In the preferred inversion, the Paracas Peninsula shows a small amount of uplift, consistent with our model-independent two-component displacement field (Fig. 8).

6 DISCUSSION

6.1 Slip distribution

Teleseismic data indicate a total magnitude for the 2007 Pisco earthquake of $M_0$8.03, with the greatest moment release occurring 55–70 s and 40 km south of the rupture initiation. InSAR-based geodetic data resolve a single patch of slip on the subduction interface centred near the Paracas Penninsula, with a higher geodetic moment (8.27). The differences in moment may indicate aseismic slip, either due to slow rupture speeds (Kanamori & Kikuchi 1993) or rapid afterslip in the first days after the earthquake (Heki *et al.* 1997).

Both geodetic and seismological slip distributions show the peak slip to the south of the epicentre, offshore of the Paracas Penninsula, but the seismological solution places the peak slip close to the epicentre (north of the Paracas Penninsula), whereas the InSAR solution places the peak slip due west of the Paracas Penninsula. As

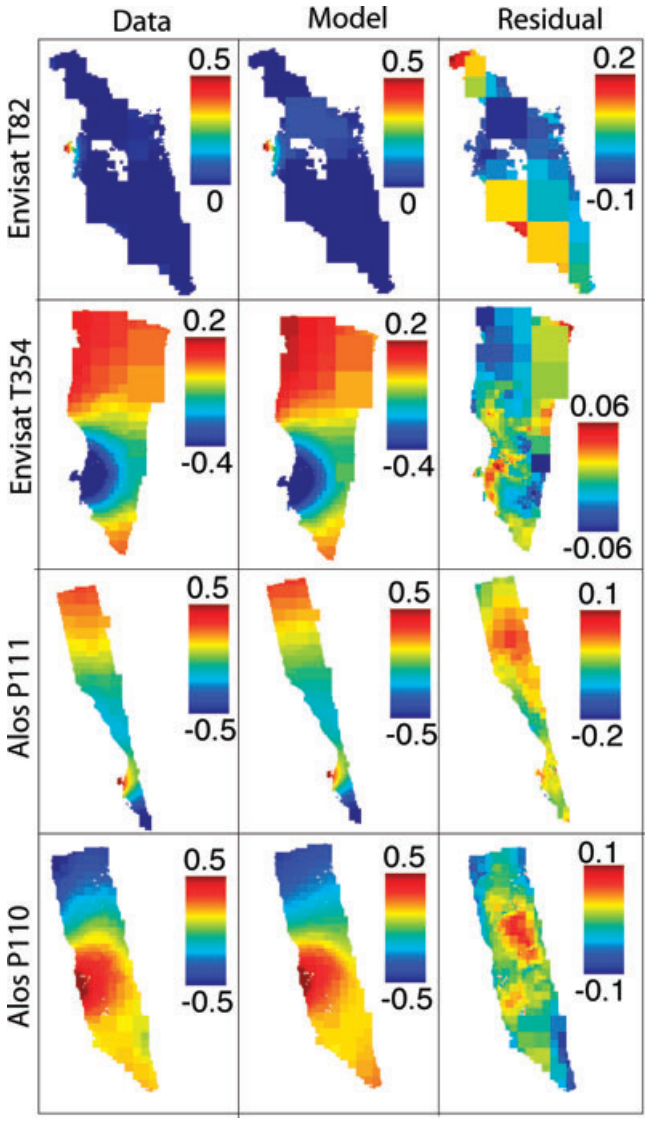

Figure 11. Interferogram, model and residual values at the subsampled points for each interferogram. The root mean square model misfits for the chosen solution (∼2.76 cm) are consistent with the magnitude expected from atmospheric noise and model geometry simplification. Note the change in colour scale between data/model and residuals.

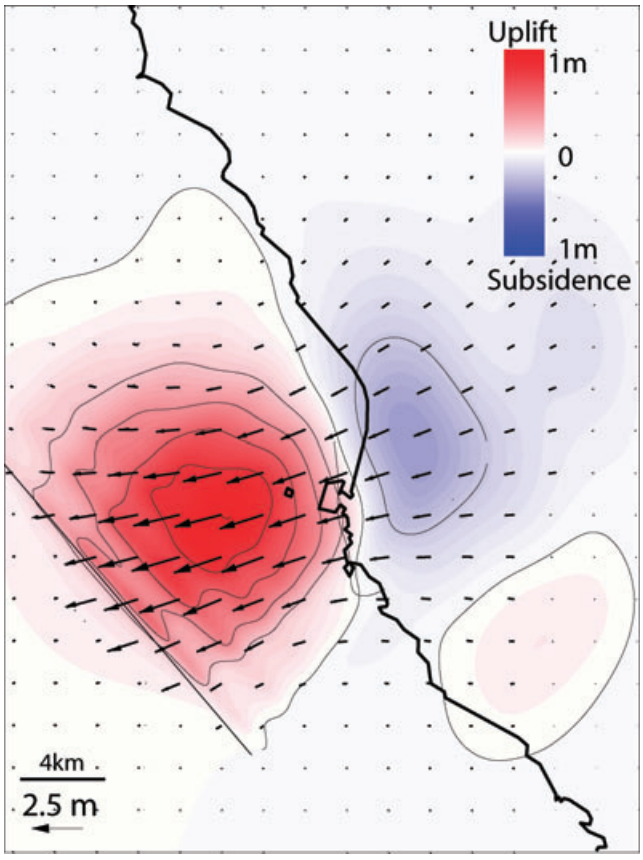

Figure 12. Model surface displacements for the 2007 Pisco, Peru earthquake. Arrows show horizontal displacements, colours shows vertical displacements with contours every 20 cm.

seen in Pritchard & Fielding (2008), the geodetic solution provides a much smoother slip distribution than the seismological solution. Resolution tests on the InSAR inversion found that due to the depth of slip, it is not possible to discriminate two separate patches, using the available geodetic data.

The patch of slip at the epicentre occurred 55–70 s earlier and 40 km further north than the main slip, effectively acting as a trigger. This appears be a common feature for large earthquakes in central Peru (Swenson & Beck 1996; Giovanni *et al.* 2002; Robinson *et al.* 2006b; Pritchard *et al.* 2007) and is a key observation for emergency response and tsunami prediction since it implies that the epicentre is likely to be several tens of kilometres north of the maximum intensities and damage.

Historical seismicity shows evidence for a curved subduction zone, with an increase in fault dip with depth; however, both our seismological and geodetic inversions find the best-fitting solutions for a single shallowly dipping fault plane. We conclude that the majority of the fault slip occurs in the upper, shallowly dipping plane, making our inversions insensitive to the geometry of the plate interface below the hinge.

It is curious that the 2006 October M6.0 and M6.7 earthquakes, which occurred very close to the 2007 August epicentre, did not trigger the same response. Based on the interseismic rates and coupling parameters of Norabuena *et al.* (1998), only an extra 3.7 cm of strain would have built-up during this time interval, less than 1 per cent of the final slip release. This situation is analogous to the 2004 Sumatra–Andaman earthquake, which was preceded by a M_w7.2 foreshock in 2002 November, which occurred close to the 2004 epicentre, but did not trigger a M9.0 earthquake (Lay *et al.* 2005).

6.2 Triggered slip on upper-plate thrusts

One striking feature of our slip distributions is the close spatial coincidence between the location of peak slip during the Pisco earthquake and anomalous topography of the Paracas Peninsula. The Peninsula consists of an oblong block 14 km long × 8 km wide, connected to the mainland by a low causeway 5 km wide. The 4 km wide Isla de Sangayan lies a further 6 km offshore. Both the peninsula and the island are composed of fault-bounded granitic blocks (Fernandez-Davilla 1975). An obvious question to ask is whether short-term, coseismic deformation has any relation to the long-term uplift of the peninsula. The obvious answer is no, in the sense that we have fit the geodetic data well with a purely elastic model, with all slip confined to the plate boundary; no permanent

deformation on additional upper plate faults is required. On the other hand, perhaps permanent deformation is small (a few percent of the coseismic deformation) or occurs offshore on upper plate faults close to the main plate boundary—in either case, difficult to observe with our data.

Stress transfer from large earthquakes has been shown to have an important influence on surrounding seismicity rates (Stein 1999). InSAR has been used to observe triggered slip on the order of 10–20 cm caused by strike-slip earthquakes (Wright *et al.* 2001; Fialko *et al.* 2002) but not yet on subduction zones. We investigate the possibility that stresses imposed on the upper plate by great earthquakes trigger activity on upper-plate thrust faults on or near the Paracas Peninsula, perhaps contributing to formation of a local topographic high. In Central Peru, historical earthquakes do not show a periodic repeat pattern, with intervals in the range 50–500 yr (Fig. 1). Based on this range of repeat times and an average uplift rate of 0.2–0.3 mm yr^{-1} (Gregory-Wodzicki 2000), a vertical component of between 1 and 15 cm of triggered slip would be required per earthquake cycle to generate the necessary uplift. This is below the size of the tidal range (40 cm) and smaller than the cracks/scarps caused by sediment slumping, hence below the resolution available from field observations (Audin *et al.* 2007) but potentially observable with InSAR.

The large-scale pattern of displacement shown in the interferograms is well modelled using slip only on the subduction interface. Close inspection of the residuals shows little to no sign of triggered slip. However, our ability to distinguish between slip on the plate interface and deformation of the upper plate depends on the nature of the deformation. Slip of 1–2 cm on a fault breaking the surface would produce less than a single fringe of range change in an Envisat interferogram and would be difficult to distinguish from subduction interface slip or atmospheric variations. Furthermore, if the uplift occurs on a buried fault, or in a distributed manner, the displacements would be smaller and cover longer wavelength making them more difficult to observe. Furthermore, the time dependence of stress transfer is poorly understood, and this area may see increased future activity over timescales of years to decades.

Subduction of aseismic ridges like the Nazca Ridge has been implicated in a number of upper plate processes that lead to long-term deformation, including significant uplift (Pilger 1981; Spikings *et al.* 2001; Hagen & Moberly 1994). Machare & Ortlieb (1992) note uplifted Plio-Quaternary marine surfaces along the Coastal Cordillera of Peru, up to 900 m in elevation, which they attribute to subduction of the Nazca Ridge. The peak uplift rate of 0.7 mm yr^{-1} (Machare & Ortlieb 1992) is clearly in excess of the long-term average uplift of 0.2–3 mm yr^{-1} (Gregory-Wodzicki 2000) required for uplift of the Andes. However, in the Pisco region, which passed over the Ridge at ∼2 Ma, the marine terraces are rare and much lower ($\leq$200 m) and appear to have been subsiding since their initial uplift during the Early Pleistocene (Machare & Ortlieb 1992). This suggests that uplift associated with ridge passage is ephemeral and that vertical motions act on a timescale of ∼1–2 Myr—intermediate between the 100–200 yr earthquake cycle and the 10–20 Myr deformation required to form the Andes.

Our results do not require any non-elastic deformation associated with the 2007 Pisco earthquake. This suggests that long-term uplift of the upper plate, including the forearc above the Nazca Ridge, must either occur aseismically or as 'slow earthquakes' during the interseismic or postseismic part of the earthquake cycle, or represents a very small fraction of coseismic deformation, below our detection threshold of 1–2 cm.

7 CONCLUSIONS

The 2007 Pisco Peru earthquake (M8.0) shows many of the characteristic features of subduction zone earthquakes in the Central Andes, including a southward propagation direction and large areas of moment release away from the epicentre. Analysis of teleseismic records indicates that the earthquake consisted of steadily increasing moment rate with the peak occurring 55–70 s and 40 km south of the epicentre. The geodetic slip distribution identifies a single large patch of slip in the location of the maximum slip associated with the peak moment rate identified by seismology.

Despite a clear spatial coincidence between the location of the coseismic slip and the anomalously high topography of the Paracas Peninsula, we find no evidence that the earthquake was directly responsible for motion on any upper-plate faults associated with shortening and uplift. The proximity to the Nazca ridge, while affecting the longer-term vertical motions, seems to have no effect on the rupture properties of the individual earthquakes, with the possible exception of a shallower dip to the subduction interface.

ACKNOWLEDGMENTS

Many thanks to Matt Pritchard and Falk Amelung for their assistance with acquiring the InSAR data. ALOS data were provided by the Alaska Satellite Facility and JAXA and Envisat imagery was acquired by ESA under the Category 1-3194 to Matt Pritchard. JB is supported by a Rosensteil Postdoctoral Fellowship at the University of Miami and a Lindemann Fellowship from the English Speaking Union. DR is supported by grant NE/C518806/1 of the Natural Environment Research Council. DPR and THD was supported by NSF-EAR 0003621. We thank M. Chlieh and one anonymous reviewer for their helpful comments. This is CSTARS contribution 19.

REFERENCES

Audin, L., Perfettini, H., Avouac, J., Farber, D., De la Cruz, D. & Chlieh, M., 2007. The 2007 pisco earthquake (M_w8.0), central Peru: preliminary field investigations and sismotectonic context, *EOS, Trans. Am. geophys. Un.,* **88**(52), T33E-02.

Bevis, M., Kendrick, E., Smalley, R., Brooks, B., Allmendinger, R. & Isacks, B., 2001. On the strength of interplate coupling and the rate of back arc convergence in the central Andes: an analysis of the interseismic velocity field, *Geochem. Geophys. Geosyst.,* **2**(11), 1067, doi:10.1029/2001GC000198.

Biggs, J., Bergman, E., Emmerson, B., Funning, G., Jackson, J., Parsons, B. & Wright, T., 2006. Fault identification for buried strike-slip earthquakes using InSAR: the 1994 and 2004 Al Hoceima, Morocco, earthquakes, *Geophys. J. Int.*, **166,** 1347–1362.

Bouchon, M. & Vallée, M., 2003. Observation of long supershear rupture during the magnitude 8.1 Kunlunshan earthquake, *Science*, **301,** 824–826.

Chlieh, M., Avouac, J.P., Sieh, K., Natawidjaja, D.H. & Galetzka, J., 2008. Heterogeneous coupling of the Sumatran megathrust constrained by geodetic and paleogeodetic measurements, *J. geophys. Res. (Solid Earth),* **113,** 5305, doi:10.1029/2007JB004981.

Das, S. & Kostrov, B.V., 1990. Inversion for seismic slip rate history and distribution with stabilizing constraints: Application to the 1986 Andreanof Islands Earthquakes, *J. geophys. Res.*, **95,** 6899–6913.

Das, S. & Kostrov, B.V., 1994. Diversity of solutions of the problem of earthquake faulting inversion. Application to *SH* waves for the great 1989 macquarie ridge earthquake, *Phys. Earth planet. Inter.*, **85,** 293–318.

Dorbath, L., Cisternas, A. & Dorbath, C., 1990. Assessment of the size of large and great historical earthquakes in peru, *Bull. seism. Soc. Am.*, **80,** 551–576.

Dunham, E. & Archuleta, R., 2004. Evidence for a supershear transient during the 2002 Denali Fault earthquake, *Bull. seism. Soc. Am.,* **96** (6B), S256–S268.

Farr, T.G. *et al.*, 2007. The shuttle radar topography mission, *Rev. Geophys.*, **45,** RG2004, doi:10.1029/2005RG000183.

Fernandez-Davilla, U., 1975. Mapa geologico del quadrangle de pisco 1:100,000, Cartas Geologica del Peru, Instituto Geologico, Minero y Metalurgico.

Fialko, Y., Sandwell, D., Agnew, D., Simons, M., Shearer, P. & Minster, B., 2002. Deformation on nearby faults induced by the 1999 Hector Mine earthquake, *Science*, **297,** 1858–1862.

Fritz, H., Kalligeris, N., Ortega, E. & Broncano, P., 2007. 15 August 2007 Peru tsunami runup and inundation, available at www.eeri.org/lfe/pdf/peru_coast_tsunami.pdf.

Funning, G., Barke, R., S.H., L., Minaya, E., Parsons, B. & Wright, T., 2005. The 1998 Aiquile, Bolivia earthquake: a seismically active fault revealed with InSAR, *Earth planet. Sci. Lett.,* **232,** 39–49.

Giovanni, M.K., Beck, S.L. & Wagner, L., 2002. The June 23, 2001 Peru earthquake and the southern Peru subduction zone, *Geophys. Res. Lett.,* **29,** 14–1, doi:10.1029/2002GL015774.

Grange, F., Hatzfeld, D., Cunningham, P., Molnar, P., Roecker, S.W., Suarez, G., Rodrigues, A. & Ocola, L., 1984. Tectonic implications of the microearthquake seismicity and fault plane solutions in southern Peru, *J. geophys. Res.*, **89,** 6139–6152.

Gregory-Wodzicki, K., 2000. Uplift history of the central and northern andes: a review, *Geol. Soc. Am. Bull.*, **112,** 1091–1105.

Hagen, R.A. & Moberly, R., 1994. Tectonic effects of a subducting aseismic ridge: the subduction of the Nazca Ridge at the Peru Trench, *Mar. geophys. Res.*, **16,** 145–161.

Heki, K., Miyazaki, S. & Tsuji, H., 1997. Silent fault slip following an interplate thrust earthquake at the Japan Trench, *Nature*, **386,** 595–598.

Henry, C., Woodhouse, J. & Das, S., 2002. Stability of earthquake moment tensor inversion: effect of the double-couple constraint, *Tectonophysics*, **356,** 115–124.

Ji, C., Wald, D. & Helmberger, D., 2002. Source description of the 1999 hector mine, California, earthquake, Part I: wavelet domain inversion theory and resolution analysis, *Bull. seism. Soc. Am.*, **92,** 1192–1207.

Jonsson, S., Zebker, H., Segall, P. & Amelung, F., 2002. Fault slip distribution of the M_w 7.2 Hector Mine earthquake estimated from satellite radar and GPS measurements, *Bull. seism. Soc. Am.*, **92,** 1377–1389.

Kanamori, H. & Kikuchi, M., 1993. The 1992 Nicaragua earthquake—a slow tsunami earthquake associated with subducted sediments, *Nature*, **361,** 714–716.

Krabbenhöft, A., Bialas, J., Kopp, H., Kukowski, N. & Hübscher, C., 2004. Crustal structure of the Peruvian continental margin from wide-angle seismic studies, *Geophys. J. Int.*, **159,** 749–764.

Lay, T. *et al.*, 2005. The great Sumatra–Andaman earthquake of 26 December 2004, *Science*, **308,** 1127–1133.

Machare, J. & Ortlieb, L., 1992. Plio-quaternary vertical motions and the subduction of the nazca ridge, central coast of Peru, *Tectonophysics*, **205,** 97–108.

Mooney, W.D., Laske, G. & Guy Masters, T., 1998. CRUST 5.1: a global crustal model at 5 deg × 5 deg, *J. geophys. Res.*, **103,** 727–748.

Norabuena, E., Leffler-Griffin, L., Mao, A., Dixon, T., Stein, S., Selwyn Sacks, I., Ocola, L. & Ellis, M., 1998. Space geodetic observations of Nazca–South America convergence across the central Andes, *Science*, **279,** 358–362.

Pilger, R., 1981. Plate reconstructions, aseismic ridges, and low-angle subduction beneath the andes, *Geol. Soc. Am. Bull.*, **92,** I448–I456.

Pritchard, M. & Fielding, E., 2008. A study of the 2006 and 2007 earthquake sequence of Pisco, Peru, with InSAR and teleseismic, *Geophys. Res. Lett.*, **35,** doi:10.1029/2008GL033374.

Pritchard, M.E., Norabuena, E.O., Ji, C., Boroschek, R., Comte, D., Simons, M., Dixon, T.H. & Rosen, P.A., 2007. Geodetic, teleseismic, and strong motion constraints on slip from recent southern Peru subduction zone earthquakes, *J. geophys. Res. (Solid Earth)*, **112**(B11), doi:10.1029/2006JB004294.

Robinson, D., Brough, C. & Das, S., 2006a. The M_w 7.8, 2001 Kunlunshan earthquake: extreme rupture speed variability and effect of fault geometry, *J. Geophys. Res. (Solid Earth),* **111**(B10), 8303, doi:10.1029/2005JB004137.

Robinson, D.P., Das, S. & Watts, A.B., 2006b. Earthquake rupture stalled by a subducting fracture zone, *Science*, **312,** 1203–1205.

Rosakis, A., Samudrala, O. & Coker, D., 1999. Cracks faster than the shear wave speed, *Science*, **284,** 1337–1340.

Rosen, P., Hensley, S., Peltzer, G. & Simons, M., 2004. Updated Repeat Orbit Interferometry package released, *EOS, Trans. Am. geophys. Un.*, **85,** 35.

Savage, J., 1983. A dislocation model of strain accumulation and release at a subduction zone, *J. geophys. Res.*, **88,** 4984–4996.

Segall, P. & Davis, J.L., 1997. GPS Applications for geodynamics and earthquake studies, *Ann. Rev. Earth planet. Sci.*, **25,** doi:/10.1146/annurev.earth.25.1.301.

Sella, G.F., Dixon, T.H. & Mao, A., 2002. REVEL: a model for recent plate velocities from space geodesy, *J. geophysi. Res. (Solid Earth)*, **107,** doi:10.1029/2000JB000033.

Spence, W., Mendoza, C., Engdahl, E.R., Choy, G.L. & Norabuena, E., 1999. Seismic subduction of the Nazca Ridge as shown by the 1996–97 Peru earthquakes, *Pure appl. Geophys.*, **154,** 753–776.

Spikings, R.A., Winkler, W., Seward, D. & Handler, R., 2001. Along-strike variations in the thermal and tectonic response of the continental Ecuadorian Andes to the collision with heterogeneous oceanic crust, *Earth planet. Sci. Lett.*, **186,** 57–73.

Stein, R.S., 1999. The role of stress transfer in earthquake occurrence, *Nature*, **402,** 605–609.

Suárez, G., Gagnepain, J., Cisternas, A., Hatzfeld, D., Molnar, P., Ocola, L., Roecker, S.W. & Viodé, J.P., 1990. Tectonic deformation of the Andes and the configuration of the subducted slab in central Peru; results from a microseismic experiment, *Geophys. J. Int.*, **103,** 1–12.

Swenson, J.L. & Beck, S.L., 1996. Historical 1942 Ecuador and 1942 Peru subduction earthquakes and earthquake cycles along Colombia-Ecuador and Peru subduction segments, *Pure appl. Geophys.*, **146,** 67–101.

Tavera, H. & Bernal, I., 2008. The pisco (peru) earthquake of 15 august 2007, *Seism. Res. Lett.*, **79,** 510–515.

Wald, D., Heaton, T. & Hudnut, K., 1996. The slip history of the 1994 northridge, California, earthquake determined from strong-motion, teleseismic, gps, and leveling data, *Bull. seism. Soc. Am.,* **86**(1B), S49–S70.

Wright, T., Parsons, B. & Fielding, E., 2001. Measurement of interseismic strain accumulation across the North Anatolian Fault by satellite radar interferometry, *Geophys. Res. Lett.*, **28**(6), 2117–2120.

Wright, T., Parsons, B. & Lu, Z., 2004. Toward mapping surface deformation in three dimensions using insar, *Geophys. Res. Lett.*, **31,** doi:10.1029/2003GL018827.